Interband chiral phonon transfer in a magnetic field

Guohuan Xiong,[1,2] Zhizhou Yu,[1,*] and Lifa Zhang[1,†]

[1]*NNU-SULI Thermal Energy Research Center (NSTER) & Center for Quantum Transport and Thermal Energy Science (CQTES), School of Physics and Technology, Nanjing Normal University, Nanjing 210023, China*

[2]*Department of Physics, National University of Singapore, Singapore 117551, Singapore*

(Received 30 September 2021; revised 18 January 2022; accepted 24 January 2022; published 31 January 2022)

Chiral phonons, which offer a possibility for information processing and storing, have been theoretically proposed and experimentally observed in two-dimensional hexagonal lattices. Here, we theoretically predict and study the interband chiral phonon transfer in a honeycomb lattice with an external magnetic field. The interband chiral phonon transfer induced by the magnetic field is accompanied by band inversions and the opening or closing of bandgaps. This can be attributed to the abrupt change of phonon band topology from the calculations of Berry curvature and Chern number. Moreover, the signs of phonon magnetic moments contributed by two optical or acoustic bands tend to be the same when a magnetic field is applied, which leads to the increasing phonon magnetic moment with the increasing strength of the magnetic field. The transfer of phonon pseudoangular momentum is also obtained due to the interband chiral phonon transfer in magnetic fields. Our findings enrich the exploration of chiral phonons and may offer theoretical guidance on the potential manipulation of chiral phonons by the external magnetic field.

DOI: 10.1103/PhysRevB.105.024312

I. INTRODUCTION

Recently, the intrinsic chirality of phonons in the absence of a magnetic field has been theoretically proposed at the Brillouin zone (BZ) corner of an asymmetric two-dimensional (2D) honeycomb lattice [1]. It was then experimentally verified in monolayer tungsten diselenide through indirect infrared absorption [2]. Like the chirality of electrons, chiral phonons can be endowed with the quantized pseudoangular momentum (PAM) owing to the threefold rotational symmetry at the high-symmetry points, which determines the selection rules of intervalley scattering of electrons [1,3–5]. Thus, the chiral phonon is potentially significant for the control of intervalley scattering [6–15], electronic phase transition [16,17], topological states [18,19], electrical resistivity of ferromagnetic metals [20], and anomalous thermal expansion [21]. In addition, since the rotation of chiral phonons is locked by the momentum of particles, it can provide a potential mechanism to process and store information by manipulating the rotation direction [2,22].

So far, chiral phonons have been theoretically studied in 2D hexagonal lattices [23–27], 2D kagome lattices [28], and some three-dimensional systems [29–31] with breaking inversion symmetry. It has been reported that, in a center-stacked bilayer triangle lattice, the phonon chirality is robust for different mass ratios of sublattices and interlayer couplings [32]. Meanwhile, the chirality of phonons can be reversed by varying interatomic interaction and doping mass in the kagome lattice [28] and the $\sqrt{3} \times \sqrt{3}$ honeycomb lattice [33], respectively. Moreover, the phonon chirality was also studied in the one-dimensional atomic junction model by using the scattering boundary method, and it was suggested that the phonon chirality can be tuned by controlling the interfacial transmitted [34] and reflected [35] waves through the interfacial materials. Recently, 40% purely circular chiral phonons have been achieved in strained graphene, and their signs can be reversed by tuning from electron to hole doping [22]. Apart from material parameters, is there a more convenient way, such as applying an external magnetic field, to manipulate chiral phonons? This is still an open question.

On the other hand, the topological behavior has been intensively investigated in phononic systems [18,36–41], which requires breaking time-reversal symmetry. Various theoretical approaches have been proposed to break the time-reversal symmetry of phonons such as the spin-lattice interaction in magnetic materials and the external magnetic field [27,39,42,43]. Although a phonon is a neutral excitation, it can weakly couple with the external magnetic field by the Lorentz force on charged ions [37,39,44,45], leading to the experimental observation of phonon Hall effect in paramagnetic dielectric $Tb_3Ga_5O_{12}$ [46,47]. Moreover, since the topological properties of phonons are strongly determined by time-reversal symmetry, chiral phonons may exhibit much more different features in systems with a magnetic field. The exploration of this issue and the related potential applications are of critical importance.

In this paper, the interband chiral phonon transfer due to the external uniform magnetic field in a 2D honeycomb lattice is studied. We find the chiral phonon transfers among bands along with band inversions and the closing or opening of bandgaps, which can be attributed to the discontinuous changes of the phonon band topology from the calculations

*yuzhizhou@njnu.edu.cn
†phyzlf@njnu.edu.cn

of Berry curvature and Chern number. Then the corresponding minimum nonzero critical magnetic field strengths are estimated in real materials. We also investigate the phonon magnetic moment for systems with different magnetic fields. It is found that the phonon magnetic moment increases linearly with the increasing magnetic field strength. Moreover, due to the interband chiral phonon transfer, the transfer of phonon PAM can be induced by the external magnetic field as well, which makes it possible to observe the interband chiral phonon transfers during electron-phonon scattering or phonon-involved optical processes.

II. MODEL AND METHOD

To study chiral phonons in a magnetic field, we consider a 2D honeycomb lattice model with two sublattices in each unit cell. This model has been extensively used to study general characteristics of chiral phonons in 2D hexagonal systems such as graphene [48,49], hexagonal boron nitride [50], and other graphenelike materials [51–54]. For an ionic crystal lattice, in the presence of a uniform magnetic field applied along the z direction, the neutral phonons are indirectly coupled with the magnetic field by the Lorentz force on charged ions. The Hamiltonian can be written as [37,39,44,45]

$$H = \frac{1}{2}\sum_{\alpha nj} m_j^{-1}(p_{\alpha nj} - q_j A_{\alpha nj})^2 + \frac{1}{2}\sum_{\alpha nj,\beta n'j'} u_{\alpha nj} K_{\alpha nj,\beta n'j'} u_{\beta n'j'}. \quad (1)$$

Here, m_j and q_j are the mass and charge of the jth atom in the unit cell, respectively. Also, $u_{\alpha nj}$ is the αth component of the displacement of the jth atom in the nth unit cell from its equilibrium position, and $p_{\alpha nj}$ is the corresponding momentum. Further, $K_{\alpha nj,\beta n'j'}$ is the atomic force constant of the lattice. As well, $A_{\alpha nj}$ is the αth component of the vector potential $\mathbf{A}_{nj}$ defined as $\mathbf{A}_{nj} = \boldsymbol{\lambda} \cdot \mathbf{u}_{nj}$, where $\boldsymbol{\lambda}$ is proportional to the applied magnetic field $\mathbf{B}$.

Then the phonon eigenmode:

$$\epsilon = (x_1, y_1, x_2, y_2)^T, \quad (2)$$

satisfies

$$[(-i\omega + \Lambda)^2 + D]\epsilon = 0. \quad (3)$$

Here,

$$D(\mathbf{k}) = -\Lambda^2 + \sum_{n'} K_{n,n'} \exp[i(\mathbf{R}_{n'} - \mathbf{R}_n)\cdot\mathbf{k}], \quad (4)$$

represents the dynamic matrix as a function of the wave vector $\mathbf{k}$. Here, $K_{n,n'}$ is the spring constant matrix between unit cell n and n'. Also, $\mathbf{R}_n$ is the real-space lattice vector. Further, Λ is a block diagonal matrix, with

$$\Lambda_j = \begin{pmatrix} 0 & h_j & -h_j & 0 \end{pmatrix}, \quad (5)$$

where

$$h_j = -\frac{\lambda q_j}{m_j}. \quad (6)$$

Here, h_j has a dimension of frequency, which can be assumed to be proportional to the magnetic field. Under the mean-field approximation, one can set $h_j = h$, which can be estimated from phonon dispersion or phonon Hall effect for a paramagnetic material [55,56]. Then the applied magnetic field λ in our model calculation can be obtained from Eq. (6). Moreover, since $\Lambda^T = -\Lambda$, the first term $-\Lambda^2$ in Eq. (4) naturally makes the dynamic matrix $D(\mathbf{k})$ positive definite. Note that there are both positive and negative ions in one unit cell. For simplicity, we only consider the 2D lattice motion; thus, the dimensions of both D and Λ are 4×4.

Now we introduce a set of right- and left-handed circular polarization as

$$\begin{aligned} |R_1\rangle &\equiv \frac{1}{\sqrt{2}}(1 \quad i \quad 0 \quad 0)^T, \\ |L_1\rangle &\equiv \frac{1}{\sqrt{2}}(1 \quad -i \quad 0 \quad 0)^T, \\ |R_2\rangle &\equiv \frac{1}{\sqrt{2}}(0 \quad 0 \quad 1 \quad i)^T, \\ |L_2\rangle &\equiv \frac{1}{\sqrt{2}}(0 \quad 0 \quad 1 \quad -i)^T. \end{aligned} \quad (7)$$

In the above basis, the operator of phonon circular polarization along the z direction can be defined as

$$\hat{S}^z \equiv \sum_{j=1}^{2}(|R_j\rangle\langle R_j| - |L_j\rangle\langle L_j|) = \begin{pmatrix} 0 & -i \\ i & 0 \end{pmatrix} \otimes I_{2\times 2}. \quad (8)$$

The corresponding phonon circular polarization is given by [1]

$$s^z_{ph} = \epsilon^\dagger \hat{S}^z \epsilon \hbar. \quad (9)$$

The circular polarization contributed by each sublattice in one unit cell is $s^z_j = \epsilon^\dagger \hat{S}^z_j \epsilon\hbar$, with $\hat{S}^z_j = |R_j\rangle\langle R_j| - |L_j\rangle\langle L_j|$. For a positive circular polarization, the phonon mode is right-handed; for a negative circular polarization, the phonon mode is left-handed; otherwise, it is static.

The phonon polarization s^z_{ph} is directly associated with the phonon angular momentum along the z direction, which has the same form as the phonon angular momentum $l^z_{\mathbf{k},\sigma}$ of the σth band at the wave vector $\mathbf{k}$ along the z direction. In equilibrium, the phonon angular momentum of one unit cell can be obtained by [55]

$$J^z_{ph} = \sum_{\sigma,\mathbf{k}} l^z_{\mathbf{k},\sigma}\left[f(\omega_{\mathbf{k},\sigma}) + \frac{1}{2}\right], \quad (10)$$

where $l^z_{\mathbf{k},\sigma} = \epsilon^\dagger_{\mathbf{k},\sigma}\hat{S}^z\epsilon_{\mathbf{k},\sigma}\hbar$ and $f(\omega_{\mathbf{k}}) = 1/[\exp(\hbar\omega_{\mathbf{k}}/k_BT) - 1]$ is the Bose-Einstein distribution.

For the sublattice with nonzero Born effective charge tensor $\mathbf{Z}^*_j$, the circular motion of each atom could induce a magnetic moment $\mu^z_{\mathbf{k},\sigma,j} = \gamma_j l^z_{\mathbf{k},\sigma,j}$ at the wave vector $\mathbf{k}$ of the σth band, where $\gamma_j = e\mathbf{Z}^*_j/(2m_j)$ is the gyromagnetic ratio of the ion [57]. Therefore, we can obtain

$$\mu^z_{\mathbf{k},\sigma,j} = \gamma_j \epsilon^\dagger_{\mathbf{k},\sigma}\hat{S}^z_j\epsilon_{\mathbf{k},\sigma}\hbar. \quad (11)$$

Then the magnetic moment $\mu^z_{\mathbf{k},\sigma}$ in each unit cell can be given by [58,59]

$$\mu^z_{\mathbf{k},\sigma} = \sum_{j=1}^{2} \mu^z_{\mathbf{k},\sigma,j} = \epsilon^{\dagger}_{\mathbf{k},\sigma} \chi \epsilon_{\mathbf{k},\sigma} \hbar, \tag{12}$$

where $\chi = \begin{pmatrix} 0 & -i \\ i & 0 \end{pmatrix} \otimes \begin{pmatrix} \gamma_1 & 0 \\ 0 & \gamma_2 \end{pmatrix}$. Finally, the total magnetic moment in one unit cell can be obtained

$$M^z_{ph} = \sum_{\sigma,\mathbf{k}} \mu^z_{\mathbf{k},\sigma} \left[f(\omega_{\mathbf{k},\sigma}) + \frac{1}{2} \right]. \tag{13}$$

To study the phonon Berry curvature, we redefine the phonon eigenmode $\epsilon'_j = \exp(-i\mathbf{d}_j \cdot \mathbf{k})\epsilon_j$, where $\mathbf{d}_j$ is the equilibrium position of the jth atom relative to the center of the unit cell. The corresponding dynamical matrix becomes

$$D'_{jj'}(\mathbf{k}) = -\Lambda^2 + \sum_{\mathbf{R}_{n'} - \mathbf{R}_n} K_{nj,n'j'} \times \exp\left[i(\mathbf{R}_{n'} - \mathbf{R}_n + \mathbf{d}_{j'} - \mathbf{d}_j) \cdot \mathbf{k} \right]. \tag{14}$$

Here, $K_{nj,n'j'}$ is the spring constant matrix between the jth atom in unit cell n and the j'th atom in unit cell n'. Analogous to the electron Berry curvature, the phonon Berry curvature can be expressed as [39]

$$\Omega^{\sigma}_{k_x k_y} = \sum_{\sigma' \neq \sigma} \frac{i}{4\omega_\sigma \omega'_\sigma} \frac{\epsilon'^{\dagger}_{\sigma} \frac{\partial D'}{\partial k_x} \epsilon'_{\sigma'} \epsilon'^{\dagger}_{\sigma'} \frac{\partial D'}{\partial k_y} \epsilon'_{\sigma} - (k_x \leftrightarrow k_y)}{\left(\omega^2_\sigma - \omega^2_{\sigma'}\right)}. \tag{15}$$

Here, all positive and negative branches are considered. Then the Chern number can be obtained from the integral of Berry curvature over the first BZ:

$$C^{\sigma} = \frac{1}{2\pi} \int_{\mathrm{BZ}} dk_x dk_y \Omega^{\sigma}_{k_x k_y} = \frac{2\pi}{L^2} \sum_{\mathbf{k}} \Omega^{\sigma}_{k_x k_y}, \tag{16}$$

where L is the length of the system.

III. RESULTS AND DISCUSSION

A. Interband chiral phonon transfer

We first calculate the phonon dispersion relation for the honeycomb lattice with $m_A = 1.0$, $m_B = 1.2m_A$, $q_A = 1.0$, and $q_B = -q_A$. The longitudinal and transverse spring constants are $k_L = 1.0$ and $k_T = 0.25k_L$, respectively. The unit cell vectors are $(a, 0)$ and $(a/2, \sqrt{3}a/2)$. These parameters used in our calculation are the same as those in Ref. [1], which can be widely used to study graphenelike monolayer ionic materials [52], such as monoxide BeO and monochloride NaCl. In the absence of a magnetic field, owing to the breaking inversion symmetry and preserved time-reversal symmetry, the valley phonon modes are nondegenerate, as shown in Fig. 1(a). From the eigenvector calculation, the phonon vibrations of two sublattices and the phonon polarization contributed by each sublattice can be obtained. Here, we only take the phonon polarization contributed from sublattice A (s^z_A) as an example. The phonon polarization s^z_A reaches its maximum value at both valleys, except for that of band 2, which reaches its minimum value with $s^z_A = 0$. All the valley phonon vibrations are circularly polarized, as depicted in the insets of Fig. 1(a). The valley phonon modes of bands 1 and 4

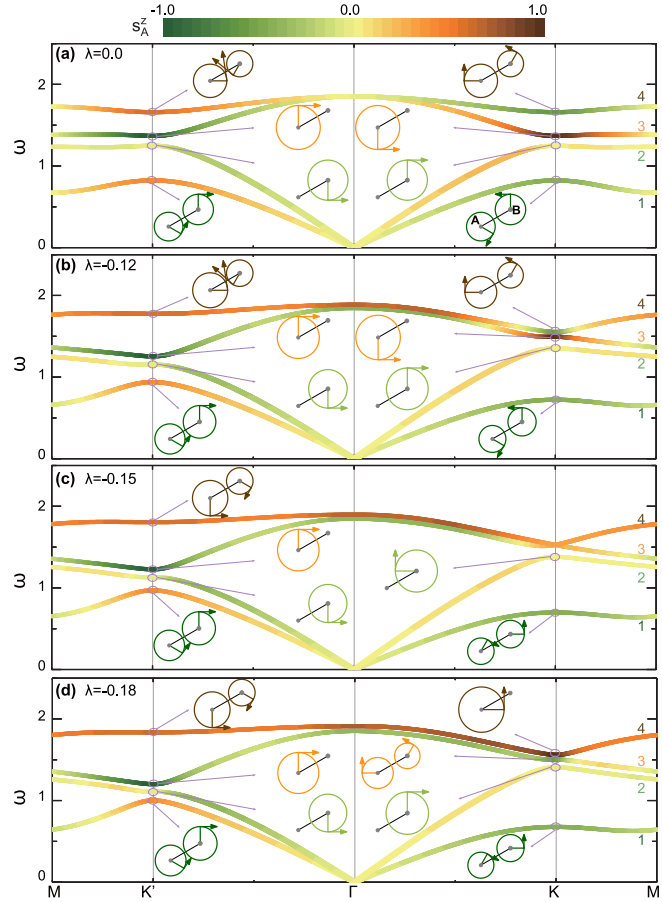

FIG. 1. Phonon dispersion relation of a honeycomb lattice for (a) $\lambda = 0.0$, (b) $\lambda = -0.12$, (c) $\lambda = \lambda_{-c1} = -0.15$, and (d) $\lambda = -0.18$. The brown and green colors represent $s^z_A > 0$ and $s^z_A < 0$, respectively. The insets show the phonon vibrations of sublattices A and B at the K point ($k_x = 4\pi/3a$ and $k_y = 0$). The radius of each circle represents the vibration amplitude. The phase and rotation direction are also included. Here, the parameters of the honeycomb lattice are set as $m_A = 1.0$, $m_B = 1.2$, $k_L = 1.0$, $k_T = 0.25k_L$, $q_A = 1.0$, and $q_B = -q_A$. The primitive vectors are $(a, 0)$ and $(a/2, \sqrt{3}a/2)$.

show opposite circular motions for different sublattices. From valley K to K', all the phonon circular motions turn to the opposite direction in this condition. The results we discussed above for the honeycomb lattice without a magnetic field agree with those reported in Ref. [1].

Moreover, when a magnetic field with $\lambda < 0$ is applied, two optical bands (bands 3 and 4) tend to touch each other at the K point, as shown in Figs. 1(a)–1(c). When λ decreases to the critical point $\lambda_{-c1} = -0.15$, the degenerate mode of two optical bands emerges in the absence of extreme value of s^z_A at the K point, as shown in Fig. 1(c). When λ further decreases, the two optical bands are separated from each other again with s^z_A changing its sign at the K point [see Fig. 1(d)], which implies that an extreme value of s^z_A reappears at the valley K. From the insets of Fig. 1(d), it can also be found that the phonon vibrations at the K point of optical bands exchange with each other except for their phases and amplitudes compared with those in the case of $\lambda \in (\lambda_{-c1}, 0]$. This also

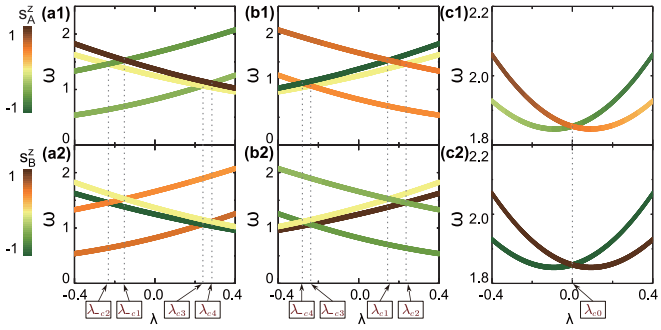

FIG. 2. Interband chiral phonon transfers at high-symmetry points. (a) λ dependence of the phonon frequency at the K point ($k_x = 4\pi/3a$, $k_y = 0$). (b) λ dependence of the phonon frequency at the K' point ($k_x = -4\pi/3a$, $k_y = 0$). (c) λ dependence of the phonon frequency at the Γ point ($k_x = 0$, $k_y = 0$) for two optical bands. The brown and green colors represent the positive and negative phonon polarization, respectively. All critical points of the magnetic field are labeled

means that, before and after the critical parameter λ_{-c1}, band inversion occurs at valley K. However, within the magnetic field shown in Fig. 1, the rotation directions of the chiral phonons at the valley K' remain unchanged.

We then calculate the phonon frequency as a function of λ at the high-symmetry points K, K', and Γ. In addition to the critical point λ_{-c1} mentioned above, more critical magnetic fields with interband chiral phonon transfers are found. At the valley K, as indicated in Fig. 2(a), the interband chiral phonon transfer also occurs at λ_{-c2}, λ_{c3}, and λ_{c4}. For sublattice A, in the condition of $\lambda < 0$, chiral phonons with negative phonon polarization s_A^z tend to possess lower frequencies, while those with positive or zero s_A^z tend to have higher frequencies. In the condition of $\lambda > 0$, chiral phonons for sublattice A show the opposite tendency. For sublattice B, the chiral phonon of each frequency at valleys always has a different polarization sign with that in sublattice A. Since the frequency of each chiral phonon varies monotonically with the magnetic field, they degenerate at λ_{-c1}, λ_{-c2}, λ_{c2}, and λ_{c4}. Thus, band inversions at the valley K take place, and chiral phonon transfers among bands happen before and after these critical points. When $\lambda < \lambda_{-c2}$, it is found that the chiral phonons of two acoustic bands in each sublattice show the same circular rotation directions due to the applied magnetic field. For systems with $\lambda > \lambda_{c4}$, the rotation directions of chiral phonons of two acoustic (optical) bands are the same as those of two optical (acoustic) bands for systems with $\lambda < \lambda_{-c2}$.

The behavior of phonon frequency and phonon polarization for systems with different λ at the K' point is like that at the K point. From Figs. 2(a) and 2(b), one can obtain that $\omega_{K',\sigma}(\lambda) = \omega_{K,\sigma}(-\lambda)$, $s^z_{A,K'}(\lambda) = -s^z_{A,K}(-\lambda)$, and $s^z_{B,K'}(\lambda) = -s^z_{B,K}(-\lambda)$. Therefore, the interband chiral phonon transfers occur at the critical magnetic fields $\lambda = \lambda_{-c3}$, λ_{-c4}, λ_{c1}, and λ_{c2} with $\lambda_{-ci} = -\lambda_{ci}$.

At the BZ center, the phonon modes of two optical bands for systems without a magnetic field are degenerated due to the time-reversal symmetry. When the applied magnetic field breaks the time-reversal symmetry, a phononic gap opens at the Γ point between two optical bands, leading to the emergence of chiral phonons, as shown in Fig. 2(c). The phonon modes of both sublattices in each optical band show the same rotation direction at the Γ point. This behavior is quite different from those of systems at the valleys. In the case of $\lambda > 0$, chiral phonons with negative phonon polarizations possess higher frequencies, while for $\lambda < 0$, chiral phonons with positive phonon polarizations have higher frequencies. However, the frequency of chiral phonons in both cases increases with the magnetic field strength.

To estimate the corresponding critical magnetic field strengths, we set $k_L = 1.44\ \text{eV/Å}^2$, $a = 1$ Å, $m_1 = 10$ u, $m_2 = 12$ u, and $q_A = e$. We also set $h_j = h$ under the mean-field approximation. In an ionic paramagnetic insulator $Tb_3Ga_5O_{12}$, the parameter h can be estimated to be 3×10^9 Hz at $B = 1$ T and $T = 5.45$ K [43]. Then the corresponding minimum nonzero critical magnetic field can be estimated as $\lambda_{c1} = 1.8 \times 10^4$ T. One can also estimate the critical parameters from the phonon dispersion since the previous theoretical study shows that the degenerate phonon modes split with a gap of $2h$ at Γ point [55]. According to the Raman scattering experiment reported in paramagnetic CeF_3 [60,61], the parameter h can be estimated as 0.39 THz at $B = 6$ T and $T = 1.9$ K. Thus, the minimum nonzero critical magnetic field strength for paramagnetic CeF_3 is $\sim 1.3 \times 10^3$ T. Although the critical magnetic fields we estimate here are quite large, one could observe the transfer in a much smaller magnetic field when materials have strong spin-phonon interaction, such as some ferromagnetic materials [25,62,63]. For instance, an infrared experiment in ferromagnetic $CdCr_2S_4$ shows that the phonon gap reaches $\sim 58\ \text{cm}^{-1}$ at $B = 7$ T and $T = 200$ K [64] so that the minimum nonzero critical magnetic field strength can be reduced to ~450 T with an estimated h of 0.87 THz.

B. Phonon magnetic moment

As mentioned in Sec. II, the phonon polarization is associated with the phonon angular momentum. Therefore, the interband chiral phonon transfers at the high-symmetry points can induce the exchange of phonon angular momentum $l^z_{\mathbf{k},\sigma}$ between two bands at the critical magnetic field. Once the Born effective charges of two sublattices are nonzero, a nonzero magnetic moment in the unit cell can be generated from the chiral phonon vibrations. According to the acoustic sum rule, the Born effective charge is set to be $Z^*_A = -Z^*_B = q_A$.

In the absence of a magnetic field, like the behavior of phonon polarization [1], the phonon magnetic moment $\mu^z_{\mathbf{k},\sigma}$ of each band reaches a maximum value at the K and K' valleys, and it is zero at the Γ point, as shown in Fig. 3(a). However, there are anions and cations in one unit cell, and the chiral phonons contributed by anions and cations exhibit different rotation directions at the valleys. The phonon magnetic moment $\mu^z_{\mathbf{k},\sigma}$ is found to have the same sign with the phonon polarization of cations in sublattice A. Therefore, from Figs. 2(a2) and 2(b2), it can be found that the sign of the magnetic moments of bands 2 and 3 is opposite to that of bands 1 and 4 at the K and K' valleys. Moreover, the phonon magnetic moment for systems without a magnetic field satisfies $\mu^z_{-\mathbf{k},\sigma} = -\mu^z_{\mathbf{k},\sigma}$, resulting in a zero magnetic moment of

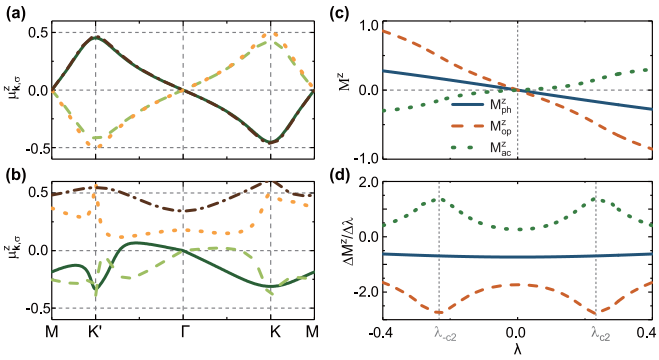

FIG. 3. Phonon magnetic moments $\mu^z_{\mathbf{k},\sigma}$ for (a) $\lambda = 0.0$ and (b) $\lambda = -0.30$. (c) Phonon magnetic moment M^z_{ph} as a function of λ at zero temperature. The solid, dashed, dotted, and dash-dotted lines correspond to bands 1 to 4, respectively. The Born effective charge is set to be $Z^*_A = -Z^*_B = q_A = -q_B$. All phonon magnetic moments are in units of $\hbar \frac{q_A}{2m_A}$.

optical bands M^z_{op} and acoustic bands M^z_{ac}, and further a zero total magnetic moment M^z_{ph}, as depicted in Fig. 3(c).

When a magnetic field is applied, owing to the interband chiral phonon transfers in sublattices, the phonon magnetic moment $\mu^z_{\mathbf{k},\sigma}$ exchanges between two bands at the critical magnetic fields, which leads to the opposite sign of phonon magnetic moment between acoustic bands and optical bands, as shown in Fig. 3(b). Moreover, since $\mu^z_{-\mathbf{k},\sigma} \neq -\mu^z_{\mathbf{k},\sigma}$ due to the time-reversal symmetry breaking, a nonzero total magnetic moment M^z_{ph} is introduced for systems with a magnetic field. Figure 3(c) presents that the total phonon magnetic moment raises linearly with the increasing strength of the magnetic field with an almost constant increasing rate $\triangle M^z_{ph} / \triangle \lambda$.

We also find that the phonon magnetic moment of the optical bands decreases, while that of the acoustic bands with the opposite contribution increases, as the magnetic field increases. In addition, it is found that the change rate of the magnetic moments M^z_{op} and M^z_{ac} reaches the fastest at $\lambda = \lambda_{\pm c2}$, at which the interband chiral phonon transfer occurs between bands 2 and 3, as shown in Fig. 3(d).

C. Berry curvature and Chern number

To further investigate the interband chiral phonon transfers of phonons in the honeycomb lattice, we calculate the phonon Berry curvatures around the critical magnetic fields. Taking the critical point λ_{-c1} as an example, the Berry curvatures of the systems with $\lambda = \lambda_{-c1} + 0.1$ and $\lambda = \lambda_{-c1} - 0.1$ are plotted in Figs. 4(a)–4(h). It is found that the Berry curvatures of two optical bands around the high-symmetry K point exhibit opposite signs before and after the critical point of the magnetic field, while those of the acoustic bands remain the same.

The Chern numbers for systems with different magnetic fields are also calculated. From Fig. 4(i), it can be found that the Chern number abruptly jumps at all critical points which are symmetrically distributed about $\lambda = 0$. Note that $\lambda = 0$ is also one of the critical points. The chiral phonon transfers at the critical magnetic field can be attributed to

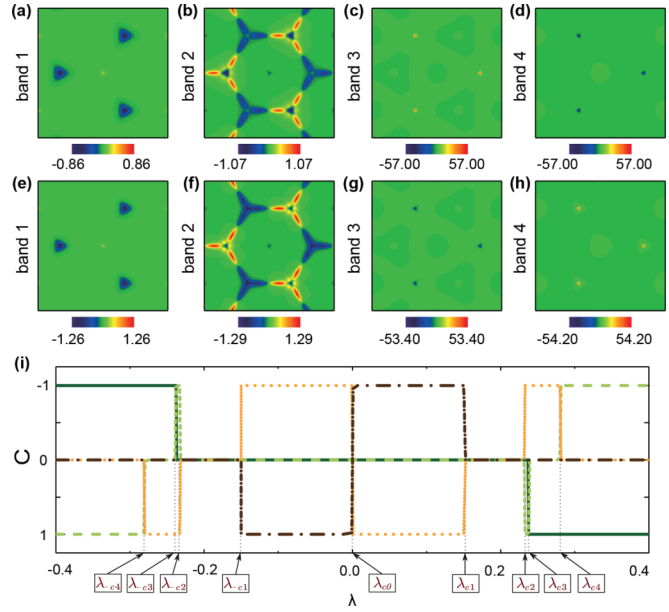

FIG. 4. (a)–(d) The contour map of phonon Berry curvatures for bands 1 to 4 at $\lambda = \lambda_{-c1} + 0.1$. (e)–(h) The contour map of phonon Berry curvatures for bands 1 to 4 at $\lambda = \lambda_{-c1} - 0.1$. (i) Chern number as a function of λ for bands 1 to 4. The solid, dashed, dotted, and dash-dotted lines represent C^1, C^2, C^3, and C^4, respectively. All critical points of the magnetic field are labeled.

the significant change of the topology of phonon bands. For instance, the Chern number of band 3 (band 4) changes from 1 (-1) to 0 at the critical point λ_{-c1} when the magnetic field λ becomes $< \lambda_{-c1}$, indicating that the topology of the optical bands abruptly changes at the critical magnetic field, which gives rise to the interband chiral phonon transfers at the valley K.

D. Phonon PAM

The phase correlation of the phonon wave function $u_{\mathbf{k}}$ not only comes from the phonon eigenvector $\epsilon_{\mathbf{k},\sigma}$ but also comes from the Bloch phase factor $\exp(i\mathbf{R}_n \cdot \mathbf{k})$. The former contributed to the local part of phonon PAM, whereas the latter represents the nonlocal part. In a honeycomb lattice, phonons at the K point present a discrete threefold rotational symmetry. Therefore, the phonon PAM $l^{\mathbf{k}}_{ph}$ at the K point can be defined as $\Re[(2\pi/3), z]u_{\mathbf{k}} = \exp[-i(2\pi/3)l^{\mathbf{k}}_{ph}]u_{\mathbf{k}}$ with the threefold rotation operator $\Re[(2\pi/3), z]$ [1,28]. The allowed values of the phonon PAM here are ± 1 and 0. We can also define the spin PAM l^s for the local part and the orbital PAM l^o for the nonlocal part in a honeycomb lattice.

The calculated phonon PAM for the sublattice A of the honeycomb lattice with different magnetic field is listed in Fig. 5(b). For systems with $\lambda_{-c1} < \lambda < \lambda_{c3}$, the phonon PAM at the K point is $+1$ for band 2, -1 for band 3, and 0 for the other two bands. To better understand the phonon PAM, we then calculate the corresponding spin and orbital PAMs. As shown in Fig. 5(a), the orbital PAMs of sublattices A and B at the K point are $l^o_A = 1$ and $l^o_B = -1$, respectively. From Eq. (7), it can be found that the right- and left-handed circular polarization are eigenstates of the threefold rotation

(a)

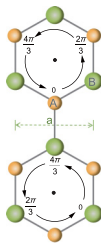

(b)

Phonon PAM at Valley K

band \ λ	$(-\infty,\lambda_{-c2})$	$(\lambda_{-c2},\lambda_{-c1})$	$(\lambda_{-c1},\lambda_{c3})$	$(\lambda_{c3},\lambda_{c4})$	$(\lambda_{c4},+\infty)$
1	0	0	0	1	1
2	0	1	1	0	-1
3	1	0	-1	-1	0
4	-1	-1	0	0	0

FIG. 5. (a) Phase correlation of the phonon nonlocal part at the valley K for the sublattice A (upper panel) and the sublattice B (lower panel). (b) Phonon pseudoangular momentum (PAM) for bands 1 to 4 at the valley K.

operator $\Re[(2\pi/3), z]$ with $l_R^s = 1$ and $l_L^s = -1$, respectively. Therefore, one can obtain $l_A^s = -1$ for bands 1 and 4 at the K points, leading to a zero phonon PAM $l_{ph} = 0$ for these two bands. Similarly, we can obtain $l_{ph} = 1$ for band 2 with $l_A^s = 0$ and $l_{ph} = -1$ for band 3 with $l_A^s = 1$.

Owing to the interband chiral phonon transfer between two bands, the phonon PAM of corresponding bands exchanges with each other at the critical point of the magnetic field. For instance, the interband chiral phonon transfer between two optical bands occurs at the critical point λ_{-c1}. Therefore, the phonon PAM of band 3 changes from $l_{ph} = -1$ at $\lambda_{-c1} < \lambda < \lambda_{c3}$ to $l_{ph} = 0$ at $\lambda_{-c2} < \lambda < \lambda_{c1}$ and that of band 4 changes from $l_{ph} = 0$ to $l_{ph} = -1$, while the phonon PAM of two acoustic bands remains the same at the critical point λ_{-c1}, as presented in Fig. 5(b).

Experimentally, chiral phonons have been successfully observed via an optical pump-probe technique [2]. As the selection rule of intervalley scattering is determined by the conservation of the PAM [1], interband chiral phonon transfers are expected to be observed during electron-phonon scattering or phonon-involved optical processes in certain ferromagnetic materials within terahertz technology.

IV. CONCLUSIONS

In summary, we have studied the chiral phonons manipulated by the magnetic field in a 2D honeycomb lattice. The interband chiral phonon transfers are found with band inversions and the closing or opening of the bandgap, which can be explained by the abrupt change of Chern numbers. For the chiral phonons of each optical band induced by the magnetic field, they show the same rotation direction in different sublattices at the Γ point, while their rotation directions at the valleys in different sublattices are opposite. Moreover, the signs of phonon magnetic moments contributed by two optical (acoustic) bands tend to be the same when the magnetic field is applied. The total phonon magnetic moment increases linearly with the increasing strength of the applied magnetic field. The increasing rates of the phonon magnetic moment contributed by the optical and acoustic bands reach the maximum at the critical points $\lambda_{\pm c2}$ where the interband chiral phonon transfer occurs between the optical and acoustic bands. In addition, the interband chiral phonon transfer leads to the transfer of phonon PAM in magnetic fields. Our results may provide theoretical guidance on the potential manipulations of chiral phonon manipulations and enrich the related phononic applications.

ACKNOWLEDGMENTS

The authors are grateful to Jun Zhou and Xiao Li for valuable discussions. This paper was supported by the National Natural Science Foundation of China (Grants No. 11890703 and No. 12074190). G.X. acknowledges the financial support from China Scholarship Council.

[1] L. Zhang and Q. Niu, Phys. Rev. Lett. **115**, 115502 (2015).
[2] H. Zhu, J. Yi, M.-Y. Li, J. Xiao, L. Zhang, C.-W. Yang, R. A. Kaindl, L.-J. Li, Y. Wang, and X. Zhang, Science **359**, 579 (2018).
[3] C. Chen, X. Chen, B. Deng, K. Watanabe, T. Taniguchi, S. Huang, and F. Xia, Phys. Rev. B **103**, 035405 (2021).
[4] H. Chen, W. Zhang, Q. Niu, and L. Zhang, 2D Mater. **6**, 012002 (2018).
[5] Y. Tatsumi, T. Kaneko, and R. Saito, Phys. Rev. B **97**, 195444 (2018).
[6] C. M. Gilardoni, F. Hendriks, C. H. van der Wal, and M. H. D. Guimarães, Phys. Rev. B **103**, 115410 (2021).
[7] T. Yin, K. A. Ulman, S. Liu, A. Granados del Águila, Y. Huang, L. Zhang, M. Serra, D. Sedmidubsky, Z. Sofer, S. Y. Quek *et al.*, Adv. Mater. **33**, 2101618 (2021).
[8] A. Delhomme, D. Vaclavkova, A. Slobodeniuk, M. Orlita, M. Potemski, D. Basko, K. Watanabe, T. Taniguchi, D. Mauro, C. Barreteau *et al.*, 2D Mater. **7**, 041002 (2020).
[9] M. He, P. Rivera, D. Van Tuan, N. P. Wilson, M. Yang, T. Taniguchi, K. Watanabe, J. Yan, D. G. Mandrus, H. Yu *et al.*, Nat. Commun. **11**, 618 (2020).
[10] Z. Li, T. Wang, S. Miao, Z. Lian, and S.-F. Shi, Nanophotonics **9**, 1811 (2020).
[11] Z. Li, T. Wang, S. Miao, Y. Li, Z. Lu, C. Jin, Z. Lian, Y. Meng, M. Blei, T. Taniguchi *et al.*, Nat. Commun. **11**, 3104 (2020).
[12] Z. Li, T. Wang, C. Jin, Z. Lu, Z. Lian, Y. Meng, M. Blei, M. Gao, T. Taniguchi, K. Watanabe *et al.*, ACS Nano **13**, 14107 (2019).
[13] Q. Guo, T. Fu, J. Tang, D. Pan, S. Zhang, and H. Xu, Phys. Rev. Lett. **123**, 183903 (2019).
[14] E. Liu, J. van Baren, T. Taniguchi, K. Watanabe, Y.-C. Chang, and C. H. Lui, Phys. Rev. Research **1**, 032007(R) (2019).
[15] X. Chen, X. Lu, S. Dubey, Q. Yao, S. Liu, X. Wang, Q. Xiong, L. Zhang, and A. Srivastava, Nat. Phys. **15**, 221 (2019).
[16] T. F. Nova, A. Cartella, A. Cantaluppi, M. Först, D. Bossini, R. V. Mikhaylovskiy, A. V. Kimel, R. Merlin, and A. Cavalleri, Nat. Phys. **13**, 132 (2017).
[17] M. Rini, R. Tobey, N. Dean, J. Itatani, Y. Tomioka, Y. Tokura, R. W. Schoenlein, and A. Cavalleri, Nature (London) **449**, 72 (2007).
[18] H. L. Calvo, J. S. Luna, V. Dal Lago, and L. E. F. Foa Torres, Phys. Rev. B **98**, 035423 (2018).

[19] G. Jotzu, M. Messer, R. Desbuquois, M. Lebrat, T. Uehlinger, D. Greif, and T. Esslinger, Nature (London) **515**, 237 (2014).
[20] E. Solano-Carrillo, Phys. Status Solidi B **255**, 1800013 (2018).
[21] C. P. Romao, Phys. Rev. B **100**, 060302(R) (2019).
[22] J. Sonntag, S. Reichardt, B. Beschoten, and C. Stampfer, Nano Lett. **21**, 2898 (2021).
[23] H. Wang, Z. Zhou, H. Chen, C. Xia, L. Zhang, and X. Li, J. Phys.: Condens. Matter **33**, 285704 (2021).
[24] W. Zhang, A. Srivastava, X. Li, and L. Zhang, Phys. Rev. B **102**, 174301 (2020).
[25] L. Du, J. Tang, Y. Zhao, X. Li, R. Yang, X. Hu, X. Bai, X. Wang, K. Watanabe, T. Taniguchi *et al.*, Adv. Funct. Mater. **29**, 1904734 (2019).
[26] M. Gao, W. Zhang, and L. Zhang, Nano Lett. **18**, 4424 (2018).
[27] D. Liu and J. Shi, Phys. Rev. Lett. **119**, 075301 (2017).
[28] H. Chen, W. Wu, S. A. Yang, X. Li, and L. Zhang, Phys. Rev. B **100**, 094303 (2019).
[29] A. Ptok, A. Kobiałka, M. Sternik, J. Łażewski, P. T. Jochym, A. M. Oleś, S. Stankov, and P. Piekarz, Phys. Rev. B **104**, 054305 (2021).
[30] H. Chen, W. Wu, J. Zhu, S. A. Yang, and L. Zhang, Nano Lett. **21**, 3060 (2021).
[31] J. Kishine, A. S. Ovchinnikov, and A. A. Tereshchenko, Phys. Rev. Lett. **125**, 245302 (2020).
[32] X. Xu, W. Zhang, J. Wang, and L. Zhang, J. Phys.: Condens. Matter **30**, 225401 (2018).
[33] X. Xu, H. Chen, and L. Zhang, Phys. Rev. B **98**, 134304 (2018).
[34] J. Wang, H. Chen, G. Xiong, X. Xu, and L. Zhang, New J. Phys. **20**, 073006 (2018).
[35] G. Xiong, Z. Yu, J.-S. Wang, and L. Zhang, New J. Phys. **21**, 093046 (2019).
[36] X. Li, C. Xia, Y. Pan, M. Gao, H. Chen, and L. Zhang, Phys. Rev. B **104**, 054103 (2021).
[37] Y. Liu, Y. Xu, S.-C. Zhang, and W. Duan, Phys. Rev. B **96**, 064106 (2017).
[38] Y. Liu, C.-S. Lian, Y. Li, Y. Xu, and W. Duan, Phys. Rev. Lett. **119**, 255901 (2017).
[39] L. Zhang, J. Ren, J.-S. Wang, and B. Li, Phys. Rev. Lett. **105**, 225901 (2010).
[40] S. Park and B.-J. Yang, Nano Lett. **20**, 7694 (2020).
[41] J. Li, L. Wang, J. Liu, R. Li, Z. Zhang, and X.-Q. Chen, Phys. Rev. B **101**, 081403(R) (2020).
[42] T. Saito, K. Misaki, H. Ishizuka, and N. Nagaosa, Phys. Rev. Lett. **123**, 255901 (2019).
[43] L. Sheng, D. N. Sheng, and C. S. Ting, Phys. Rev. Lett. **96**, 155901 (2006).
[44] J.-S. Wang and L. Zhang, Phys. Rev. B **80**, 012301 (2009).
[45] A. Holz, Nuov. Cim. B **9**, 83 (1972).
[46] A. V. Inyushkin and A. Taldenkov, JETP Lett. **86**, 379 (2007).
[47] C. Strohm, G. L. J. A. Rikken, and P. Wyder, Phys. Rev. Lett. **95**, 155901 (2005).
[48] S. Chen, Q. Wu, C. Mishra, J. Kang, H. Zhang, K. Cho, W. Cai, A. A. Balandin, and R. S. Ruoff, Nat. Mater. **11**, 203 (2012).
[49] S. Y. Zhou, G.-H. Gweon, A. Fedorov, P. N. First, W. De Heer, D.-H. Lee, F. Guinea, A. C. Neto, and A. Lanzara, Nat. Mater. **6**, 770 (2007).
[50] G. Kim, A.-R. Jang, H. Y. Jeong, Z. Lee, D. J. Kang, and H. S. Shin, Nano Lett. **13**, 1834 (2013).
[51] C. Xia, W. Li, D. Ma, and L. Zhang, Nanotechnology **31**, 375705 (2020).
[52] B. Luo, Y. Yao, E. Tian, H. Song, X. Wang, G. Li, K. Xi, B. Li, H. Song, and L. Li, Proc. Natl. Acad. Sci. USA **116**, 17213 (2019).
[53] H. R. Gutiérrez, N. Perea-López, A. L. Elías, A. Berkdemir, B. Wang, R. Lv, F. López-Urías, V. H. Crespi, H. Terrones, and M. Terrones, Nano Lett. **13**, 3447 (2013).
[54] K. F. Mak, C. Lee, J. Hone, J. Shan, and T. F. Heinz, Phys. Rev. Lett. **105**, 136805 (2010).
[55] L. Zhang and Q. Niu, Phys. Rev. Lett. **112**, 085503 (2014).
[56] L. Zhang, J.-S. Wang, and B. Li, New J. Phys. **11**, 113038 (2009).
[57] D. M. Juraschek and N. A. Spaldin, Phys. Rev. Materials **3**, 064405 (2019).
[58] D. M. Juraschek, M. Fechner, A. V. Balatsky, and N. A. Spaldin, Phys. Rev. Materials **1**, 014401 (2017).
[59] J. Eshbach and M. Strandberg, Phys. Rev. **85**, 24 (1952).
[60] K. Ahrens and G. Schaack, Phys. Rev. Lett. **42**, 1488 (1979).
[61] G. Schaack, Solid State Commun. **17**, 505 (1975).
[62] Y. Tian, M. J. Gray, H. Ji, R. Cava, and K. S. Burch, 2D Mater. **3**, 025035 (2016).
[63] M. Iliev, H. Guo, and A. Gupta, Appl. Phys. Lett. **90**, 151914 (2007).
[64] T. Rudolf, C. Kant, F. Mayr, J. Hemberger, V. Tsurkan, and A. Loidl, Phys. Rev. B **76**, 174307 (2007).